

# Region-wise Loss for Biomedical Image Segmentation

Juan Miguel Valverde, Jussi Tohka\*

*A.I. Virtanen Institute for Molecular Sciences, University of Eastern Finland, 70150 Kuopio, Finland*

---

## Abstract

We propose Region-wise (RW) loss for biomedical image segmentation. Region-wise loss is versatile, can simultaneously account for class imbalance and pixel importance, and it can be easily implemented as the pixel-wise multiplication between the softmax output and a RW map. We show that, under the proposed Region-wise loss framework, certain loss functions, such as Active Contour and Boundary loss, can be reformulated similarly with appropriate RW maps, thus revealing their underlying similarities and a new perspective to understand these loss functions. We investigate the observed optimization instability caused by certain RW maps, such as Boundary loss distance maps, and we introduce a mathematically-grounded principle to avoid such instability. This principle provides excellent adaptability to any dataset and practically ensures convergence without extra regularization terms or optimization tricks. Following this principle, we propose a simple version of boundary distance maps called rectified RW maps that, as we demonstrate in our experiments, achieve state-of-the-art performance with similar or better Dice coefficients and Hausdorff distances than Dice, Focal, and Boundary losses in three distinct segmentation tasks. We quantify the optimization instability provided by Boundary loss distance maps, and we empirically show that our rectified RW maps are stable to optimize. The code to run all our experiments is publicly available at: <https://github.com/jmlipman/RegionWiseLoss>.

**Keywords:** Deep Learning, Segmentation, Medical Imaging, Loss Function

---

## 1. Introduction

Image segmentation is a typical pre-processing step required for quantitative image analyses in biomedical applications. Accurate segmentation is crucial to measure, for instance, brain tumor size, which can determine the radiation dose administered to patients during radiotherapy [1]. Since segmenting images manually is time consuming and subjective [2, 3, 4], there is a great interest in developing reliable tools to segment medical images automatically.

Convolutional neural networks (ConvNets) have shown excellent performance in multiple segmentation tasks, be-

coming widely employed in biomedical image segmentation competitions [5, 6, 7]. Due to the idiosyncrasies of medical images, accounting for pixel importance and class imbalance can be critical to produce accurate segmentations. To achieve this, a common strategy is to simultaneously minimize multiple terms or loss functions that consider different aspects, such as class imbalance or pixel importance. As an example, Taghanaki et al. [8] combined Cross Entropy loss with Dice loss to tackle class imbalance, and Gerl et al. [9] combined Cross Entropy with a domain-specific penalty term. However, minimizing multiple loss functions or terms requires extra hyper-parameters to balance the individual contribution of each loss function, as loss functions yield values in different ranges, which, in turn, affect the gradients during back-propagation. As a consequence, costly hyper-parameter tuning becomes necessary. Furthermore, en-

---

\*Corresponding author

Email address:

{juanmiguel.valverde, jussi.tohka}@uef.fi (Juan Miguel Valverde, Jussi Tohka)

tangling multiple losses makes unclear whether a specific loss function *alone* or the extra terms were responsible for tackling, e.g., class imbalance. In this paper, we propose Region-wise (RW) loss, a general framework capable of jointly considering class imbalance and pixel importance without additional hyper-parameter or loss functions.

We show that several widely used loss functions, including Active contour (AC) [10], Hausdorff distance (HD) [11] and Boundary [12] losses, can be reformulated as RW losses, revealing their underlying similarities. Besides, Boundary and HD losses are reportedly unstable to optimize and, as explained in [11, 12], it is necessary to combine them with Dice loss to circumvent such optimization instability. However, it is unclear if specifically Dice loss should be paired with Boundary or HD losses to achieve stable optimization and, more importantly, the exact cause of this optimization instability has remained unknown. Kervadec et al. [12] hypothesized that the optimization of boundary distance maps occasionally fails because empty foregrounds (all zeroes in the foreground class) produce small gradients. This hypothesis describes a typical class imbalance scenario where the majority of the pixels outweigh foreground pixels and, consequently, the few foreground pixels contribute little to the gradients. In this paper, we explain, utilizing the RW loss framework, why these loss functions are unstable to optimize, and we introduce a mathematically-grounded principle that leads to optimization stability.

Our contributions are the following:

- We present RW loss, a loss function that is unique in its ability to simultaneously account for class imbalance and pixel importance.
- We show that certain important loss functions (AC [10], HD [11] and Boundary [12] losses) are special cases of RW loss.
- We analyze RW loss and provide theoretical and empirical insight of the cause of the observed—yet not understood—instability: gradient vectors with incorrect signs.
- We introduce a principle to fix the optimization instability, and we derived our simple rectified RW maps (Fig. 1, (d)) that, in contrast to other special cases of RW loss, utilize boundary distance maps

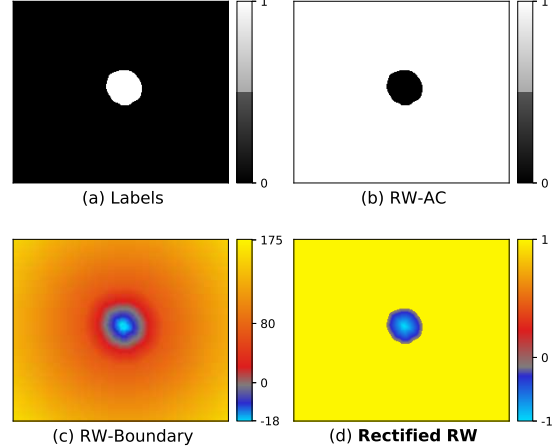


Figure 1: Representative visualization of a single channel of the ground truth (a) and its corresponding RW maps (b-c-d). (a) One-hot encoded matrix. (b) RW Active contour map. (c) RW Boundary distances map. (d) Our proposed normalized rectified RW map, with normalized negative distances in the foreground and ones in the background.

while ensuring optimization stability with no additional loss functions, regularization terms, or optimization tricks.

- We show that RW loss with our proposed rectified RW maps achieved state-of-the-art performance, producing similar or better Dice coefficients and Hausdorff distances than Dice, Focal and Boundary losses on three large biomedical datasets [5, 6, 13].
- We compared previous strategies to circumvent optimization instability with Boundary loss, and we show that, regardless of the strategy, our rectified RW maps led to less fluctuations during the optimization and provided convergence faster.

## 2. Related work

*Segmentation with class imbalance.* Class imbalance occurs when pixels from a certain class outnumber other classes, a common scenario in medical imaging segmentation (e.g., tumor vs. non-tumor). One simple method to

tackle class imbalance is to assign higher weights to foreground classes, as in weighted Cross Entropy loss. Focal loss [14] modifies Cross Entropy to reduce the effect of high softmax probability values and it accentuates pixels with smaller softmax probabilities. Several loss functions have been inspired by widely used segmentation performance metrics, including Dice loss [15, 16], Tversky loss [17], Jaccard loss [18], Lovász-Softmax loss [19], and HD loss [11]. Active contour (AC) loss [10], inspired by the classical Chan-Vese formulation of active contour models [10], also focuses on the foreground classes. AC loss divides the images into foreground and background and, as we detail in the next section, it maximizes the predicted probability values of true positives and negatives while considering the length of the predicted boundary.

*Boundary distance maps.* In medical imaging segmentation, misclassification severity can depend on pixel location. Frequently, misclassifications near the segmentation boundaries are less severe than those farther apart, since these boundaries can be ambiguous to denote. Hausdorff distance quantifies this misclassification severity by measuring the largest segmentation error. Boundary loss [12], similarly to HD loss [11], penalizes heavily misclassifications far from the segmentation boundaries with boundary distance maps (Fig 1 (c)). Wang et al. [20] employed these boundary distance maps to gradually align ground truth’s boundaries with the prediction’s. Caliva et al. [21] reversed boundary distance map values by assigning more importance to areas near the segmentation boundaries. Gerl et al. [9] incorporated prior knowledge about the epidermis shape through a distance-based smoothness penalty term. Notably, the aforementioned works employed distance-based loss functions that were unstable to optimize and, to circumvent such instability, extra loss functions were also optimized, as suggested in [12]. Furthermore, certain optimization strategies, such as in Boundary loss [12], update hyper-parameters after every epoch and, consequently, are heavily affected by the training set size, as smaller training sets perform less iterations per epoch, leading to faster hyper-parameter updates. Motivated by the reliance of these loss functions on creative optimization strategies and extra hyper-parameters, we investigated their instability and, based on our analyses, propose our rectified RW maps that require no extra loss functions or hyper-parameters while utilizing

boundary distance maps.

### 3. Region-wise loss

#### 3.1. Definition and gradients

Let  $\mathbf{x} \in \mathbb{R}^N$  be a vectorized image and  $\mathbf{Y} = (y)_{ik} \in \{0, 1\}^{N \times K}$  be the one-hot encoded matrix of its labels where  $N$  and  $K$  are the number of pixels and classes, respectively. For simplicity, we restrict our notation to a single image channel. Let  $\Phi = (\phi)_{ik} = [\phi_1, \dots, \phi_N]$  denote the unnormalized prediction of a ConvNet (i.e., logits) and  $\hat{\mathbf{Y}} = (\hat{y})_{ik} = [\hat{y}_1, \dots, \hat{y}_N]$  its softmax normalized values, widely used in semantic segmentation due to the validity of such probability values. We define Region-wise (RW) loss as the sum of the element-wise multiplication between the softmax probability values and a RW map  $\mathbf{Z} = (z)_{ik} = [z_1, \dots, z_N]$ . Formally<sup>1</sup>:

$$L_{RW} = \sum_{i=1}^N \hat{y}_i^\top \mathbf{z}_i = \sum_{i=1}^N \sigma(\phi_i)^\top \mathbf{z}_i \quad (1)$$

where  $\phi_i$ ,  $\hat{y}_i$  and  $\mathbf{z}_i$  are  $K$ -length column vectors and  $\sigma$  is the softmax function. This formulation extends [12] and it is not limited to a specific RW map. RW maps are computed as  $\mathbf{Z} = f(\mathbf{Y})$  where  $f : \{0, 1\}^{N \times K} \rightarrow \mathbb{R}^{N \times K}$ . Importantly,  $\mathbf{Z}$  depends on the ground truth and is independent of the network’s parameters. Figure 1 (b-c-d) shows three examples of RW maps. Region-wise loss yields the following gradients:

$$\frac{\partial L_{RW}}{\partial \phi_{ik}} = \hat{y}_{ik} \sum_{l=1, l \neq k}^K \hat{y}_{il} (z_{ik} - z_{il}). \quad (2)$$

The full derivation can be found in Section A of the Supplementary Material.

#### 3.2. Properties

Region-wise loss is versatile, and other loss functions can be reformulated as a RW loss. Region-wise loss generalizes Boundary loss [12] that employs RW maps defined as the Euclidean distance to segmentation bound-

<sup>1</sup>For notational convenience, we define RW loss as a sum, but in practice, we normalize it by multiplying with  $(NK)^{-1}$ .

aries. We refer to these RW maps as RW-Boundary maps (Fig. 1 (c)), and they are defined as

$$z_{ik} = \begin{cases} -\|i - b_{ik}\|_2 & \text{if } i \in \Omega_k \\ \|i - b_{ik}\|_2 & \text{otherwise} \end{cases}, \quad (3)$$

where  $\Omega_k$  is the foreground area of class  $k$ , and  $b_{ik}$  is the closest ground-truth boundary pixel to  $i$  in class  $k$ . Likewise, HD loss that uses distance maps as Boundary loss can also be reformulated as RW loss. Active contour (AC) loss  $L_{AC}$  [10], inspired by active contour models, combines the regions inside and outside the ground truth foreground  $\Omega$  with the *length* of the mask perimeter (or surface, in 3D images):  $L_{AC} = \text{length} + \lambda(R_{in} + R_{out})$ , where  $R_{in} = \sum_{i \in \Omega} \hat{y}_{il}$  (false negatives),  $R_{out} = \sum_{i \notin \Omega} \hat{y}_{il}$  (false positives), and 1 and 2 refer to the background and foreground channels, respectively. Defining the RW map as  $z_i = [0, 1]^T$  if  $i \in \Omega$  and  $z_i = [1, 0]^T$  if  $i \notin \Omega$ , or, equivalently,  $\mathbf{Z} = \mathbf{1} - \mathbf{Y}$ , where  $\mathbf{1}$  is the  $N \times K$  matrix of ones, we get  $L_{AC} = \text{length} + \lambda L_{RW-AC}$  (Fig. 1, (a-b)). Intuitively, multiplying the softmax probability values by  $\mathbf{Z}$  penalizes background pixels (i.e., the false positives and negatives) in proportion to their corresponding softmax values; and because softmax probabilities sum to one, minimizing the softmax values of background pixels equates to maximizing the softmax values of the foreground area for every channel. This reformulation of AC loss into RW loss reveals its a priori non-trivial similarity with another loss function [22] that proposed non-distance maps defined as  $z_i = [-\beta, \alpha]^T$  if  $i \in \Omega$  and  $z_i = [\alpha, -\beta]^T$  if  $i \notin \Omega$ . In other words, under our RW loss framework, AC loss is the zero-one normalized version of [22].

Region-wise loss allows penalizing each predicted pixel in a certain manner based on its class *and* location. In other words, RW loss can tackle class imbalance while simultaneously considering pixel importance. For instance, RW maps can be designed to highlight boundaries between classes, or to penalize pixels far from these boundaries, depending on the nature of the segmentation task. This flexibility contrasts with other loss functions such as Cross entropy. Cross entropy can be modified to tackle class imbalance (weighted Cross entropy), and it can also be adjusted to incorporate pixel-wise-specific information [23]. However, incorporating weights similar to RW maps into the Cross entropy loss to account for class imbalance and pixel importance simultaneously as

$L_{PWCE} = -\sum_{i,k}^{N,K} z_{ik} y_{ik} \log \hat{y}_{ik}$  does not guarantee that the gradients will utilize all RW map values. Since its derivative  $\frac{\partial L_{PWCE}}{\partial \Phi_{ik}} = -z_{ik} y_{ik} + \hat{y}_{ik} \sum_l z_{il} y_{il}$  multiplies one-hot encoded vectors  $\mathbf{y}_i$ , only  $z_{ik}$  is effective, where  $k$  is the true class. Consequently,  $K - 1$  values will remain unused. Thus, tackling class imbalance and pixel importance with Cross entropy without any extra term is not trivial.

### 3.3. Rectified Region-wise maps (RRW)

Region-wise maps must be corrected to ensure optimization stability. Any RW map can be rectified by enforcing ( $z_{ik} - z_{il}$ ) in Eq. (2) to be 0 for  $i \in \Omega_m, k \neq m, l \neq m$ , i.e., by setting the  $K - 1$  background values of each  $z_i$  vector to be equal for each pixel location separately. If foreground and background values are non-positive and non-negative, respectively, this definition ensures the correctness of the gradient signs, which provides stable optimization. Note that AC loss [10] that reported no optimization instability follows, inadvertently, this principle.

We applied the same principle to RW-Boundary maps (Eq. (3)) and we normalized foreground values between  $[-1, 0]$ , yielding our rectified Region-wise maps (RRW)  $\mathbf{Z}$ :

$$z_{ik} = \begin{cases} \frac{-\|i - b_{ik}\|_2}{\max_{j \in \Omega_k} \|j - b_{jk}\|_2} & \text{if } i \in \Omega_k \\ 1 & \text{otherwise} \end{cases}. \quad (4)$$

In other words, foreground values are normalized negative Euclidean distances to the boundaries (Fig. 1 (d)). This simple approach is hyper-parameter-free and yields favorable gradients in typical optimization scenarios. Furthermore, these values that cancel out  $z_{ik}, z_{il}$  also represent pixel importance and affect the computed loss. For instance, for softmax values  $\hat{y}_i = [0.25, 0.25, 0.25, 0.25]$  and RW map values  $z_i = [0, 0, 0, -0.6]$ , the gradients are  $[0.04, 0.04, 0.04, -0.11]$  and the loss becomes  $-0.04$ . In contrast, for more important pixels, setting  $\hat{y}_i = [1, 1, 1, -0.6]$ , as in our RRW maps (Eq. (4)), yields larger gradients  $[0.1, 0.1, 0.1, -0.3]$  and a loss of  $0.15$ . Since too large gradients can excessively alter ConvNets' parameters during optimization, we suggest to normalize these RW maps to facilitate training stability and convergence under the most common optimization hyper-parameters choices. Additionally, RW maps could be computed on-the-fly to apply transfer learning [24] by weighting images or certain regions, and they can be also modified to

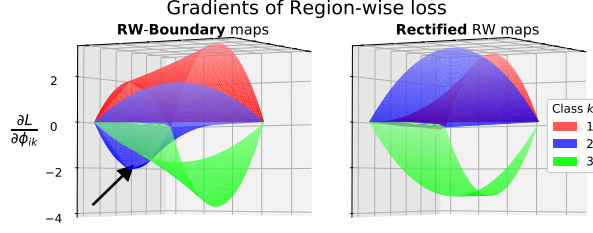


Figure 2: Gradients from RW-Boundary ( $z_i = [12, 4, -3]$ ) and rectified ( $z_i = [10, 10, -3]$ ) RW map for all possible softmax vectors  $\hat{y}_i$ . The black arrow indicates the presence of undesirable negative values in class 2 gradient vectors.

account for class imbalance by, for instance, adjusting the distance values in every channel/category.

### 3.4. Source of optimization instability

During the optimization of ConvNets with softmax at the end of their architecture, typical loss functions produce gradient vectors with one negative value and  $K - 1$  positive values. This leads the corresponding one and  $K - 1$  softmax values to increase and decrease, respectively. In contrast, certain loss functions that can be reformulated as Region-wise loss, including HD [11] and Boundary [12] losses, use RW maps that produce partial derivatives with incorrect signs. These incorrect signs arise due to the interconnections  $z_{ik}$  and  $z_{il}$  (Eq. (2)) in segmentation tasks of more than two classes. As a consequence, multiple softmax values undesirably increase at the same time, causing optimization instability.

Figure 2 shows the gradients produced by a particular  $z_i$  from RW-Boundary (left) and our RRW map (right) for all possible softmax vectors in a three-class segmentation task. As the true label is  $y_i = [0, 0, 1]$ , gradient vectors are expected to contain one negative value in class 3 (green) and two positive values in classes 1 and 2 (red and blue). However, the simulation depicted in Figure 2 (left, black arrow) shows that more than half of class 2 gradient vectors produced by the RW-Boundary map had two negative values, increasing two softmax values simultaneously. In contrast, our RRW map yielded gradients with the correct sign across all softmax vectors.

Figure 3 illustrates the number of negative values in images from two datasets used in this study (KiTS19

(top) and ACDC17 (bottom)) at three different optimization time-points in two independent training instances. Contrary to the expected single negative value per softmax vector, RW-Boundary maps produced gradient vectors  $\frac{\partial L_{RW}}{\partial \phi_i}$  with several negative values, guiding their corresponding softmax vectors to undesirably increase in multiple directions. The regions with gradients with incorrect signs (Fig. 3, negative values 2 and 3) start large and progressively shrink. However, these regions do not completely disappear, hindering the optimization.

In addition to the instability caused by certain RW maps, RW loss derivative's non-linearity produces gradients that do not always increase on par with the error, and these gradients can occasionally be too small. Although these two issues related to small and non-linear gradients can be circumvented with suitable step size, we study them to provide a deeper understanding of RW loss. Following Eq. (2), the gradients in a two-class segmentation task are:

$$\begin{aligned} \frac{\partial L_{RW}}{\partial \phi_{i1}} &= z_{i1}\hat{y}_{i1} - \hat{y}_{i1}^2 z_{i1} - \hat{y}_{i1}z_{i2}\hat{y}_{i2} \\ &= \hat{y}_{i1}(\hat{y}_{i2}(z_{i1} - z_{i2})) = \hat{y}_{i1}(1 - \hat{y}_{i1})(z_{i1} - z_{i2}). \end{aligned} \quad (5)$$

Since  $(z_{i1} - z_{i2})$  is constant, softmax values  $\hat{y}_{i1} = t$  and  $\hat{y}_{i1} = 1 - t$  with  $t \in [0, 1]$  produce the same gradient. This property is not limited to two-class segmentation. Figure 4 illustrates RW and Cross entropy loss gradients with respect to  $\phi_{i1}$  for all possible combinations of softmax values in a three-class segmentation task with  $y_i = \mathbf{1} - z_i = [1, 0, 0]$ . Cross entropy gradients (Figure 4, lower triangle) are correlated to the error: the farther  $\hat{y}_i$  is from the true label the gradient becomes more negative. In contrast, RW loss gradients (Figure 4, upper triangle) behave similarly until the saddle point at the center of the triangle where  $\frac{\partial L_{RW}}{\partial \phi_{i1}} = -0.25$  and gradients start increasing. Additionally, since the softmax value  $\hat{y}_{ik}$  (Eq. (2)) multiplies every other term of the summation, small softmax values yield small gradients, potentially hindering the optimization at the beginning when the softmax values associated to the true labels can be small. In practice, adaptive optimization algorithms, such as Adam [25], provide sufficiently good step sizes, facilitating the optimization. In fact, in our experiments, we demonstrate that optimizing RW loss is not only feasible but it also achieves state-of-the-art performance.

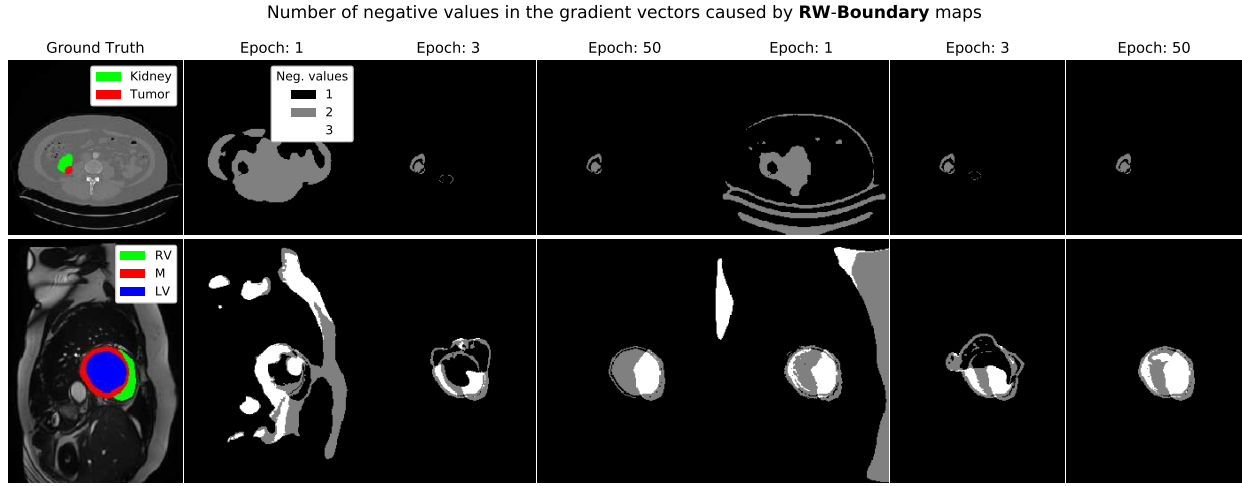


Figure 3: Number of negative values in the gradient vectors when optimizing with RW-Boundary maps. Top row: KiTS19 dataset. Bottom row: ACDC17 dataset. First column: Ground truth. Columns 2-4 and 5-7 show two independent runs at different optimization time-points.

Dataset	C	Train/Val Images	Description
ACDC17 [6]	3	100/100 (2D)	Cardiac MRI
BraTS18 [5]	3	105/105 (2D)	Brain MRI
KiTS19 [13]	2	105/105 (2D)	Kidney CT

Table 1: Data summary. C = number of foreground classes.

#### 4. Experiments

We conducted the following experiments: 1) comparing RW loss and our hyper-parameter-free rectified RW (RRW) maps with three other widely used loss functions on three large biomedical datasets; 2) studying the converge frequency provided by RW-Boundary and our RRW maps; and 3) evaluating multiple optimization strategies to achieve convergence with unrectified RW maps and our RRW maps.

**Datasets.** We conducted our experiments on Automated Cardiac Diagnosis Challenge 2017 (ACDC17) [6], Multimodal Brain Tumor Segmentation Challenge 2018 (BraTS18) [5] and Kidney Tumor Challenge 2019 (KiTS19) [13] training sets (see Table 1 for a brief overview). ACDC17 dataset comprised cardiac magnetic resonance images (MRIs) of 100 patients acquired with

different equipment. For each subject, two 3D-image frames were manually segmented into background, right ventricle (RV), myocardium (M) and left ventricle (LV). BraTS18 dataset included the 210 high-grade glioma patients, and the images were segmented into background, edema (ED), enhancing tumor core (ET) and necrotic and non-enhancing tumor core (NCR\_NET). KiTS19 dataset included 210 patients, and images were segmented into background, kidney and kidney tumor. Additionally, we resized KiTS19 image slices to 256x256 to reduce the computational costs. All images were standardized to have zero-mean unit-variance, and we divided each dataset in half: training and validation set. Note that this split is considerably more challenging than in the segmentation competitions since our training sets are much smaller.

**Model and training.** We utilized nnUNet [26], a self-configuring UNet [23] that tailors certain optimization settings and architectural components (e.g., number of filters, batch size, image crop size) to each dataset. nnUNet has achieved state-of-the-art results on several segmentation datasets [26] and, since it is based on UNet, it portrays a typical segmentation approach in biomedical image segmentation. We utilized the official implemen-

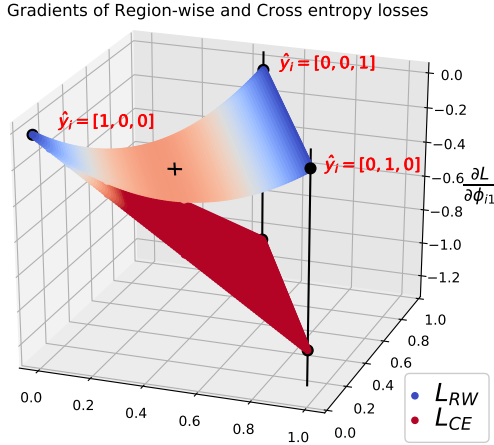


Figure 4: Gradients of Region-wise and Cross entropy losses with respect to  $\phi_{i1}$  for all possible softmax vectors  $\hat{y}_i$  in a three-class segmentation problem.  $\ddagger$ : saddle point where  $\frac{\partial L_{RW}}{\partial \phi_{i1}} = -0.25$

tation of nnUNet<sup>2</sup>; we added the evaluated loss functions (RW, Dice [15], Focal [14], Boundary loss [12]), and we employed Adam optimizer [25], as in [12], with a learning rate starting at  $10^{-5}$ . We trained nnUNet for 300 epochs in ACDC17 dataset, and 100 epochs in BraTS18 and KiTS19 datasets. The remaining optimization settings of nnUNet, including polynomial learning rate decrease and deep supervision [27], were unmodified. All the experiments were implemented in Pytorch [28], and the complete code to run all our experiments and scripts to prepare the data can be found at: <https://github.com/jmlipman/RegionWiseLoss>.

*Evaluation.* We evaluated performance with Dice coefficient [29] and Hausdorff distance [30] on non-background classes. Dice coefficient quantifies the similarity between the predictions and their ground truth

$$Dice(A, B) = \frac{2|A \cap B|}{|A| + |B|}, \quad (6)$$

<sup>2</sup><https://github.com/MIC-DKFZ/nnUNet>

where  $A$  and  $B$  are the segmentation masks. Hausdorff distance measures the largest segmentation error

$$HD(A, B) = \max \left\{ \max_{a \in \partial A} \min_{b \in \partial B} |b - a|, \max_{b \in \partial B} \min_{a \in \partial A} |a - b| \right\}, \quad (7)$$

where  $\partial A$  and  $\partial B$  are the boundary voxels of  $A$  and  $B$ , respectively. Particularly, Hausdorff distance is crucial to demonstrate that pixel importance is considered during the optimization. Since certain object boundaries can be ambiguous to delineate due to low image contrast—typical in medical images, pixels far from these boundaries are critical, and small Hausdorff distances are desired. We averaged Dice coefficients and Hausdorff distances across three independent runs and, in the experiments where we evaluated convergence separately (Section 4.3), we rerun models that failed to converge, avoiding convergence problems to interfere with performance values.

#### 4.1. Evaluation on three large datasets

We evaluated RW loss with our hyper-parameter-free RRW maps ( $L_{RW}$ , Eq. (4)) on ACDC17, BraTS18 and KiTS19 datasets. We compared our approach with Boundary loss, which combines RW-Boundary maps (Eq. 3) and Dice loss, and, as our RRW maps, also considers pixel importance via distance maps. We optimized Boundary loss following the original training setting [12], i.e., by decreasing  $\alpha$  after every epoch from 1 to 0.01 in:  $L_{Dice+Boundary} = \alpha L_{Dice} + (1 - \alpha)L_{RW}$ . Additionally, we evaluated Dice and Focal losses, two state-of-the-art loss functions that account for class imbalance. We optimized the non- $\alpha$ -balanced Focal loss function (i.e., we set  $\alpha = 1$  using notation of [14]), and we set  $\gamma = 2$ , as the original study [14] reported that this choice yielded the best results. Tables 2, 3 and 4 list the per-class Dice coefficients and Hausdorff distances, and the percentage of class voxels relative to background voxels. Moreover, we assessed whether the Dice coefficients and Hausdorff distances of the segmentations derived with our RRW maps were significantly different from those of the other studied losses through a paired permutation test with 10000 random iterations.

On average, our RRW maps produced the highest Dice coefficients and lowest Hausdorff distances on ACDC17

		Loss fun.	
		Dice	H.D.
RV 1.21 %	$L_{RRW}$	0.90 ± 0.09	14.58 ± 11.03
	$L_{Dice}$	0.87 ± 0.11*	20.98 ± 15.34*
	$L_{Focal}$	0.89 ± 0.09	14.89 ± 11.07
	$L_{Dice+Boundary}$	0.89 ± 0.09	16.55 ± 13.85
M 1.30 %	$L_{RRW}$	0.90 ± 0.03	9.01 ± 7.62
	$L_{Dice}$	0.89 ± 0.03*	13.87 ± 21.83*
	$L_{Focal}$	0.90 ± 0.03	9.90 ± 14.60
	$L_{Dice+Boundary}$	0.90 ± 0.04	8.41 ± 5.39
LV 1.27 %	$L_{RRW}$	0.94 ± 0.05	7.53 ± 5.95
	$L_{Dice}$	0.94 ± 0.05	11.40 ± 19.29*
	$L_{Focal}$	0.94 ± 0.05	8.44 ± 13.44
	$L_{Dice+Boundary}$	0.94 ± 0.06	8.36 ± 7.85

Table 2: Performance on ACDC17 dataset. Percentages indicate the proportion between class pixels and background pixels. Scores that were significantly different from  $L_{RRW}$  were marked with \* ( $p$ -value < 0.05).

		Loss fun.	
		Dice	H.D.
ET 0.26 %	$L_{RRW}$	0.80 ± 0.15	20.76 ± 19.32
	$L_{Dice}$	0.79 ± 0.16*	77.49 ± 16.67*
	$L_{Focal}$	0.80 ± 0.14	19.27 ± 18.16
	$L_{Dice+Boundary}$	0.80 ± 0.15	19.04 ± 15.58
ED 0.66 %	$L_{RRW}$	0.78 ± 0.14	37.48 ± 18.56
	$L_{Dice}$	0.77 ± 0.14	74.22 ± 13.83*
	$L_{Focal}$	0.78 ± 0.14	37.01 ± 19.25
	$L_{Dice+Boundary}$	0.78 ± 0.14	29.35 ± 18.80*
NCR_NET 0.16 %	$L_{RRW}$	0.61 ± 0.26	16.47 ± 12.64
	$L_{Dice}$	0.61 ± 0.25	61.48 ± 22.34*
	$L_{Focal}$	0.61 ± 0.26	16.16 ± 14.63
	$L_{Dice+Boundary}$	0.60 ± 0.27	16.87 ± 12.45

Table 3: Performance on BraTS18 dataset. Percentages indicate the proportion between class pixels and background pixels. Scores that were significantly different from  $L_{RRW}$  were marked with \* ( $p$ -value < 0.05).

		Loss fun.	Dice	H.D.
Kidney 1.89 %	$L_{RRW}$	0.95 ± 0.04	20.29 ± 16.64	
	$L_{Dice}$	0.94 ± 0.04*	21.02 ± 18.44	
	$L_{Focal}$	0.95 ± 0.04	19.84 ± 15.73	
	$L_{Dice+Boundary}$	0.94 ± 0.05*	18.62 ± 16.00	
Tumor 0.47 %	$L_{RRW}$	0.57 ± 0.31	56.38 ± 30.92	
	$L_{Dice}$	0.53 ± 0.31	84.29 ± 25.04*	
	$L_{Focal}$	0.51 ± 0.35*	41.37 ± 29.52*	
	$L_{Dice+Boundary}$	0.51 ± 0.33*	55.50 ± 30.48	

Table 4: Performance on KiTS19 dataset. Percentages indicate the proportion between class pixels and background pixels. Scores that were significantly different from  $L_{RRW}$  were marked with \* ( $p$ -value < 0.05).

dataset (Table 2). Dice loss yielded significantly worse results in almost all metrics and classes; Focal loss achieved similar or slightly worse results than our RRW maps; and Boundary loss also underperformed, except in the Hausdorff distances of the myocardium class. In BraTS18 and KiTS19 datasets (Tables 3 and 4), RRW maps produced similar or better Dice coefficient than the other loss functions and, mostly, significantly better Hausdorff distances than Dice loss. Focal and Boundary loss produced overall slightly better Hausdorff distances than the RRW maps, although they were usually not significantly different. Dice coefficients and Hausdorff distances inevitably differed from competition participant’s approaches [5, 6, 7] since our training-validation split was considerably more challenging (i.e., remarkably smaller training set); however, results are expected to scale with other split proportions.

Our RRW maps achieved, overall, similar or better Dice coefficients and Hausdorff distances than the other evaluated loss functions in three class-imbalanced datasets. Notably, as described in Section 4.2, our hyper-parameter-free RRW maps could be tailored to each dataset—strategy similar to hyper-parameter fine-tuning, as in Focal loss—to focus more on certain classes or regions, potentially increasing performance. However, designing dataset-specific RRW maps was beyond the scope of this paper; instead, we showed that simple RRW maps performed at least as well as other state-of-the-art loss functions. Dice loss provided segmentations with remarkably worse Hausdorff distances than the other loss functions, although such underperformance was unsur-

prisingly as Dice loss considers no pixel importance or prediction confidence, unlike the other loss functions. In addition, contrary to Boundary loss, our RRW maps require no hyper-parameter updates during the optimization as the proposed RRW maps with normalized boundary distances are stable to optimize, thus, having no reliance on the training set size. Furthermore, the validation curves, Figures 7-9 in the Supplementary Material, show that our RRW maps provided faster convergence than Dice and Boundary loss.

#### 4.2. Rectified Region-wise maps convergence

We quantified the convergence frequency of RW-Boundary maps (Eq. (3)) and our RRW maps (Eq. (4)) in nnUNet, which, in contrast to vanilla UNet, has several architectural components and training settings to facilitate the optimization, such as residual connections [31], batch normalization [32], deep supervision [27], and polynomial learning rate decrease. We trained 50 models on ACDC17 dataset for 50 epochs, as it was enough to determine whether a model failed to converge, and we calculated the empirical cumulative distribution function (CDF):

$$CDF(d) = \frac{1}{n} \sum_{i=1}^n \mathbb{1}(d_i \leq d), \quad (8)$$

where  $\mathbb{1}(c)$  is the indicator function taking the value 1 if the condition  $c$  is true and 0 if  $c$  is false. Intuitively, the CDF indicates the fraction of models that achieved a Dice coefficient of  $d$  or lower.

Figure 5 provides empirical evidence that our RRW maps lead to optimization stability, as all models trained with our RRW maps produced Dice coefficients of 0.9 or higher. In contrast, a fraction of the models optimized with RW-Boundary maps reached a suboptimal local minima due to optimization instability, producing Dice coefficients around 0.5. Furthermore, our RRW maps achieved higher Dice coefficients than RW-Boundary maps.

#### 4.3. Incorporating additional loss functions to facilitate convergence

We investigated the impact on the performance and convergence of the two strategies that previous studies utilized to circumvent the optimization instability of RW loss with RW-Boundary maps (Eq. (3)). In particular,

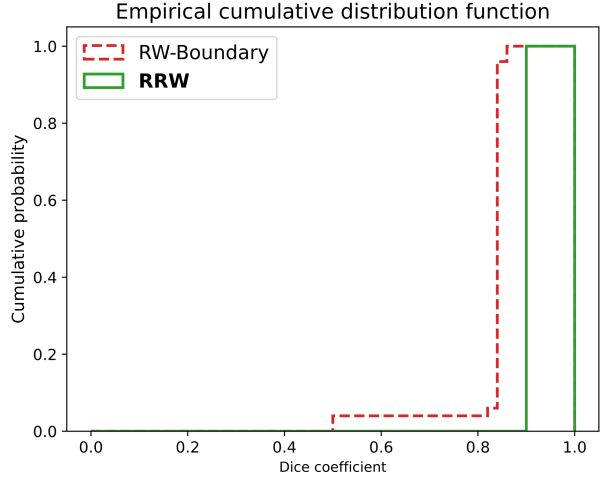


Figure 5: Empirical distribution function illustrating the fraction of models that achieved a certain Dice coefficient or lower.

we inspected the average Dice coefficient on ACDC17 dataset’s validation set during the optimization and, similarly to Section 4.2, we computed the CDF of 50 trained models for each optimization strategy. These optimization strategies were: 1) combining RW loss with Dice loss:  $L_{Dice} + L_{RW}$  [11] (*equal* contribution); and 2) gradually increasing the influence of RW loss by decreasing  $\alpha$  in:  $\alpha L_{Dice} + (1 - \alpha)L_{RW}$  [12] (*gradual* contribution). Motivated by the smoothness of Cross entropy’s derivative  $\frac{\partial L_{RW}}{\partial \phi_i} = \hat{y}_i - y_i$ , we also studied the use of Cross entropy loss instead of Dice loss. Additionally, although our RRW maps already provide stable optimization, we also evaluated the application of these strategies when optimizing RW loss with the proposed RRW maps (Eq. (4)).

Figure 6 (a) shows that, despite averaging across three independently-trained models and three foreground classes, optimizing RW-Boundary maps provided Dice coefficients that fluctuated similarly for the first 210 epochs regardless of the optimization strategy. At the end of the optimization, the evaluated strategies appear to have converged, providing similar Dice coefficients. Additionally, *gradual* contribution strategies yielded high Dice coefficients slightly faster than *equal* contribution strategies. In contrast, our RRW maps were invariant to the optimization strategy as they equally provided similar

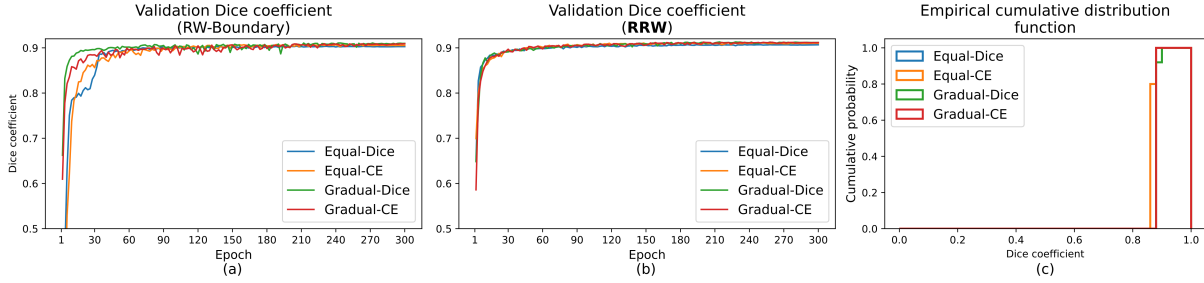


Figure 6: (a-b) Average Dice coefficient during training on ACDC17 dataset while optimizing RW loss with RW-Boundary and RRW maps following different optimization strategies to ensure convergence. (c) Empirical distribution function illustrating the convergence capability of these approaches with RW-Boundary maps.

performance, fewer oscillations and faster convergence in all optimization scenarios (see Fig. 6 (b)), corroborating the importance of rectifying RW maps.

Figure 6 (c) illustrates the CDF after optimizing 50 models with RW-Boundary maps. In contrast to optimizing RW-Boundary maps alone (Section 4.2), incorporating an additional loss function, regardless of the optimization strategy, seemed, in practice, to provide convergence. In agreement with Figure 6 (a), *gradual* contribution strategies were slightly better, increasing the Dice coefficients by a small margin.

## 5. Conclusion

We presented Region-wise loss for image segmentation, capable to jointly account for class imbalance and pixel importance. This capability allows to leverage underrepresented classes and to penalize predictions based on pixel location during the optimization. We showed that other loss functions (Active contour, Hausdorff distance and Boundary losses) can be reformulated as the presented RW-loss framework, unveiling their underlying similarities. Furthermore, our analyses of RW loss revealed the cause of the optimization instability exhibited by certain special cases of RW loss, such as Boundary loss. Based on these analyses, we derived a mathematically-grounded principle to provide optimization stability, and we proposed our RRW maps that permit utilizing boundary distance maps while requiring no extra hyper-parameters.

In our experiments, RW loss with our simple hyper-parameter-free RRW maps produced segmentations with Dice coefficients and HDs similar or better than Dice, Focal and Boundary loss functions on three class-imbalanced datasets, achieving state-of-the-art performance. Additionally, we confirmed the optimization instability suffered by Boundary loss, quantified its frequency, and empirically demonstrated that our RRW maps are stable to optimize, supporting our theoretical analysis. Finally, we evaluated multiple strategies to achieve stable optimization with unrectified RW maps and showed that our RRW maps, unlike RW-Boundary maps, barely fluctuated and converged faster.

## Acknowledgements

The work of J.M. Valverde was funded from the European Union’s Horizon 2020 Framework Programme (Marie Skłodowska Curie grant agreement #740264 (GENOMMED)). This work has also been supported by the grant #316258 from Academy of Finland (J. Tohka)

## References

- [1] M. Kim, C. S. Kay, W. I. Jang, M.-S. Kim, D. S. Lee, H. S. Jang, Prognostic value of tumor volume and radiation dose in moderate-sized hepatocellular carcinoma: A multicenter analysis in korea (krog 14–17), Medicine 96 (24).

- [2] J. M. Valverde, A. Shatillo, R. De Feo, O. Gröhn, A. Sierra, J. Tohka, Ratlesnetv2: A fully convolutional network for rodent brain lesion segmentation, *Frontiers in neuroscience* 14 (2020) 1333.
- [3] I. A. Mulder, A. Khmelinskii, O. Dzyubachyk, S. de Jong, N. Rieff, M. J. Wermer, M. Hoehn, B. P. Lelieveldt, A. M. van den Maagdenberg, Automated ischemic lesion segmentation in mri mouse brain data after transient middle cerebral artery occlusion, *Frontiers in neuroinformatics* 11 (2017) 3.
- [4] A. Zijdenbos, R. Forghani, A. Evans, Automatic quantification of ms lesions in 3d mri brain data sets: validation of insect, in: *International Conference on Medical Image Computing and Computer-Assisted Intervention*, Springer, 1998, pp. 439–448.
- [5] S. Bakas, M. Reyes, A. Jakab, S. Bauer, M. Rempfler, A. Crimi, R. T. Shinohara, C. Berger, S. M. Ha, M. Rozycki, et al., Identifying the best machine learning algorithms for brain tumor segmentation, progression assessment, and overall survival prediction in the brats challenge, *arXiv preprint arXiv:1811.02629*.
- [6] O. Bernard, A. Lalande, C. Zotti, F. Cervenansky, X. Yang, P.-A. Heng, I. Cetin, K. Lekadir, O. Camara, M. A. G. Ballester, et al., Deep learning techniques for automatic mri cardiac multi-structures segmentation and diagnosis: is the problem solved?, *IEEE transactions on medical imaging* 37 (11) (2018) 2514–2525.
- [7] N. Heller, F. Isensee, K. H. Maier-Hein, X. Hou, C. Xie, F. Li, Y. Nan, G. Mu, Z. Lin, M. Han, et al., The state of the art in kidney and kidney tumor segmentation in contrast-enhanced ct imaging: Results of the kits19 challenge, *Medical Image Analysis* 67 (2021) 101821.
- [8] S. A. Taghanaki, Y. Zheng, S. K. Zhou, B. Georgescu, P. Sharma, D. Xu, D. Comaniciu, G. Hamarneh, Combo loss: Handling input and output imbalance in multi-organ segmentation, *Computerized Medical Imaging and Graphics* 75 (2019) 24–33.
- [9] S. Gerl, J. C. Paetzold, H. He, I. Ezhov, S. Shit, F. Kofler, A. Bayat, G. Tetteh, V. Ntziachristos, B. Menze, A distance-based loss for smooth and continuous skin layer segmentation in optoacoustic images, in: *International Conference on Medical Image Computing and Computer-Assisted Intervention*, Springer, 2020, pp. 309–319.
- [10] X. Chen, B. M. Williams, S. R. Vallabhaneni, G. Czanner, R. Williams, Y. Zheng, Learning active contour models for medical image segmentation, in: *Proceedings of the IEEE Conference on Computer Vision and Pattern Recognition*, 2019, pp. 11632–11640.
- [11] D. Karimi, S. E. Salcudean, Reducing the hausdorff distance in medical image segmentation with convolutional neural networks, *IEEE transactions on medical imaging*.
- [12] H. Kervadec, J. Bouchtiba, C. Desrosiers, E. Granger, J. Dolz, I. B. Ayed, Boundary loss for highly unbalanced segmentation, *arXiv preprint arXiv:1812.07032*.
- [13] N. Heller, N. Sathianathan, A. Kalapara, E. Walczak, K. Moore, H. Kaluzniak, J. Rosenberg, P. Blake, Z. Rengel, M. Oestreich, J. Dean, M. Tradewell, A. Shah, R. Tejpal, Z. Edgerton, M. Peterson, S. Raza, S. Regmi, N. Papanikolopoulos, C. Weight, The kits19 challenge data: 300 kidney tumor cases with clinical context, ct semantic segmentations, and surgical outcomes (2019). *arXiv:arXiv:1904.00445*.
- [14] T.-Y. Lin, P. Goyal, R. Girshick, K. He, P. Dollár, Focal loss for dense object detection, in: *Proceedings of the IEEE international conference on computer vision*, 2017, pp. 2980–2988.
- [15] F. Milletari, N. Navab, S.-A. Ahmadi, V-net: Fully convolutional neural networks for volumetric medical image segmentation, in: *2016 Fourth International Conference on 3D Vision (3DV)*, IEEE, 2016, pp. 565–571.
- [16] C. H. Sudre, W. Li, T. Vercauteren, S. Ourselin, M. J. Cardoso, Generalised dice overlap as a deep learn-

- ing loss function for highly unbalanced segmentations, in: Deep learning in medical image analysis and multimodal learning for clinical decision support, Springer, 2017, pp. 240–248.
- [17] S. S. M. Salehi, D. Erdogmus, A. Gholipour, Tversky loss function for image segmentation using 3d fully convolutional deep networks, in: International Workshop on Machine Learning in Medical Imaging, Springer, 2017, pp. 379–387.
- [18] J. Bertels, T. Eelbode, M. Berman, D. Vandermeulen, F. Maes, R. Bisschops, M. B. Blaschko, Optimizing the dice score and jaccard index for medical image segmentation: Theory and practice, in: International Conference on Medical Image Computing and Computer-Assisted Intervention, Springer, 2019, pp. 92–100.
- [19] M. Berman, A. R. Triki, M. B. Blaschko, The lovász-softmax loss: A tractable surrogate for the optimization of the intersection-over-union measure in neural networks, in: Proceedings of the IEEE Conference on Computer Vision and Pattern Recognition, 2018, pp. 4413–4421.
- [20] C. Wang, Y. Zhang, M. Cui, J. Liu, P. Ren, Y. Yang, X. Xie, X. Hua, H. Bao, W. Xu, Active boundary loss for semantic segmentation, arXiv preprint arXiv:2102.02696.
- [21] F. Caliva, C. Iriondo, A. M. Martinez, S. Majumdar, V. Pedoia, Distance map loss penalty term for semantic segmentation, arXiv preprint arXiv:1908.03679.
- [22] X. Cao, H. Chen, Y. Li, Y. Peng, Y. Zhou, L. Cheng, Boundary loss with non-euclidean distance constraint for abus mass segmentation, in: 2020 13th International Congress on Image and Signal Processing, BioMedical Engineering and Informatics (CISP-BMEI), IEEE, 2020, pp. 645–650.
- [23] O. Ronneberger, P. Fischer, T. Brox, U-net: Convolutional networks for biomedical image segmentation, in: International Conference on Medical image computing and computer-assisted intervention, Springer, 2015, pp. 234–241.
- [24] S. J. Pan, Q. Yang, A survey on transfer learning, *IEEE Transactions on knowledge and data engineering* 22 (10) (2009) 1345–1359.
- [25] D. P. Kingma, J. Ba, Adam: A method for stochastic optimization, *CoRR* abs/1412.6980.
- [26] F. Isensee, P. F. Jaeger, S. A. Kohl, J. Petersen, K. H. Maier-Hein, nnu-net: a self-configuring method for deep learning-based biomedical image segmentation, *Nature Methods* 18 (2) (2021) 203–211.
- [27] C.-Y. Lee, S. Xie, P. Gallagher, Z. Zhang, Z. Tu, Deeply-supervised nets, in: Artificial intelligence and statistics, PMLR, 2015, pp. 562–570.
- [28] A. Paszke, S. Gross, F. Massa, A. Lerer, J. Bradbury, G. Chanan, et al., Pytorch: An imperative style, high-performance deep learning library, in: Advances in Neural Information Processing Systems, 2019, pp. 8024–8035.
- [29] L. R. Dice, Measures of the amount of ecologic association between species, *Ecology* 26 (3) (1945) 297–302.
- [30] G. Rote, Computing the minimum hausdorff distance between two point sets on a line under translation, *Information Processing Letters* 38 (3) (1991) 123–127.
- [31] K. He, X. Zhang, S. Ren, J. Sun, Deep residual learning for image recognition, in: Proceedings of the IEEE conference on computer vision and pattern recognition, 2016, pp. 770–778.
- [32] S. Ioffe, C. Szegedy, Batch normalization: Accelerating deep network training by reducing internal covariate shift, arXiv preprint arXiv:1502.03167.

## Supplementary Material

### A. Full derivation of Region-wise loss gradients

We derive the gradients of our Region-wise loss  $L_{RW} = \sum_{i=1}^N \hat{y}_i^\top z_i$  with respect to the unnormalized prediction of a ConvNet  $\Phi$  (i.e., the logits) that multiply every other gradient during optimization with back-propagation. These gradients can be computed by applying the chain rule:

$$\frac{\partial L_{RW}}{\partial \phi_{ik}} = \frac{\partial L_{RW}}{\partial \hat{y}_i} \frac{\partial \hat{y}_i}{\partial \phi_{ik}} \quad (9)$$

where  $\hat{y}_i$  are the ConvNet predictions at pixel  $i$  normalized by the softmax function

$$\hat{y}_i = \sigma(\phi_i) = \frac{e^{\phi_{ik}}}{\sum_{l=1}^K e^{\phi_{il}}} \quad (10)$$

First, we calculate the derivative of the softmax function with respect to the logits. The Jacobian of  $\hat{y}_i$  is:

$$\frac{\partial \hat{y}_i}{\partial \phi_i} = \begin{bmatrix} \frac{\partial \hat{y}_{i1}}{\partial \phi_{i1}} & \cdots & \frac{\partial \hat{y}_{iK}}{\partial \phi_{i1}} \\ \vdots & \ddots & \vdots \\ \frac{\partial \hat{y}_{i1}}{\partial \phi_{iK}} & \cdots & \frac{\partial \hat{y}_{iK}}{\partial \phi_{iK}} \end{bmatrix} \quad (11)$$

where, for any  $k, l$ ,

$$\frac{\partial \hat{y}_{ik}}{\partial \phi_{il}} = \frac{e^{\phi_{ik}} \sum_{l=1}^N e^{\phi_{il}} - e^{\phi_{ik}} e^{\phi_{il}}}{(\sum_{l=1}^N e^{\phi_{il}})^2} = \frac{e^{\phi_{ik}} (\sum_{l=1}^N e^{\phi_{il}} - e^{\phi_{ik}})}{(\sum_{l=1}^N e^{\phi_{il}})^2} \quad (12)$$

Following Eq. (12), if  $k = l$ :

$$\frac{\partial \hat{y}_{ik}}{\partial \phi_{il}} = \frac{e^{\phi_{ik}}}{\sum_{l=1}^N e^{\phi_{il}}} \frac{\sum_{l=1}^N e^{\phi_{il}} - e^{\phi_{ik}}}{\sum_{l=1}^N e^{\phi_{il}}} = \hat{y}_{ik} (1 - \hat{y}_{ik}) \quad (13)$$

and if  $k \neq l$ :

$$\frac{\partial \hat{y}_{ik}}{\partial \phi_{il}} = \frac{0 - e^{\phi_{il}} e^{\phi_{ik}}}{(\sum_{l=1}^N e^{\phi_{il}})^2} = -\hat{y}_{ik} \hat{y}_{il} \quad (14)$$

The derivative of our Region-wise loss with respect to the normalized predictions is

$$\frac{\partial L_{RW}}{\partial \hat{y}_i} = \sum_{l=1}^K z_{il} \quad (15)$$

Finally, by plugging Eqs. (13-14-15) into Eq. (9), we have:

$$\begin{aligned} \frac{\partial L_{RW}}{\partial \phi_{ik}} &= z_{ik} \hat{y}_{ik} (1 - \hat{y}_{ik}) + \sum_{l=1; l \neq k}^K z_{il} (-\hat{y}_{ik} \hat{y}_{il}) = z_{ik} \hat{y}_{ik} - z_{ik} \hat{y}_{ik} \hat{y}_{ik} - \sum_{l=1; l \neq k}^K z_{il} \hat{y}_{ik} \hat{y}_{il} \\ &= z_{ik} \hat{y}_{ik} - \hat{y}_{ik} \sum_{l=1}^K z_{il} \hat{y}_{il} = \hat{y}_{ik} \sum_{l=1; l \neq k}^K \hat{y}_{il} (z_{ik} - z_{il}) \end{aligned} \quad (16)$$

## B. Validation curves

### B.1. ACDC17 Dataset

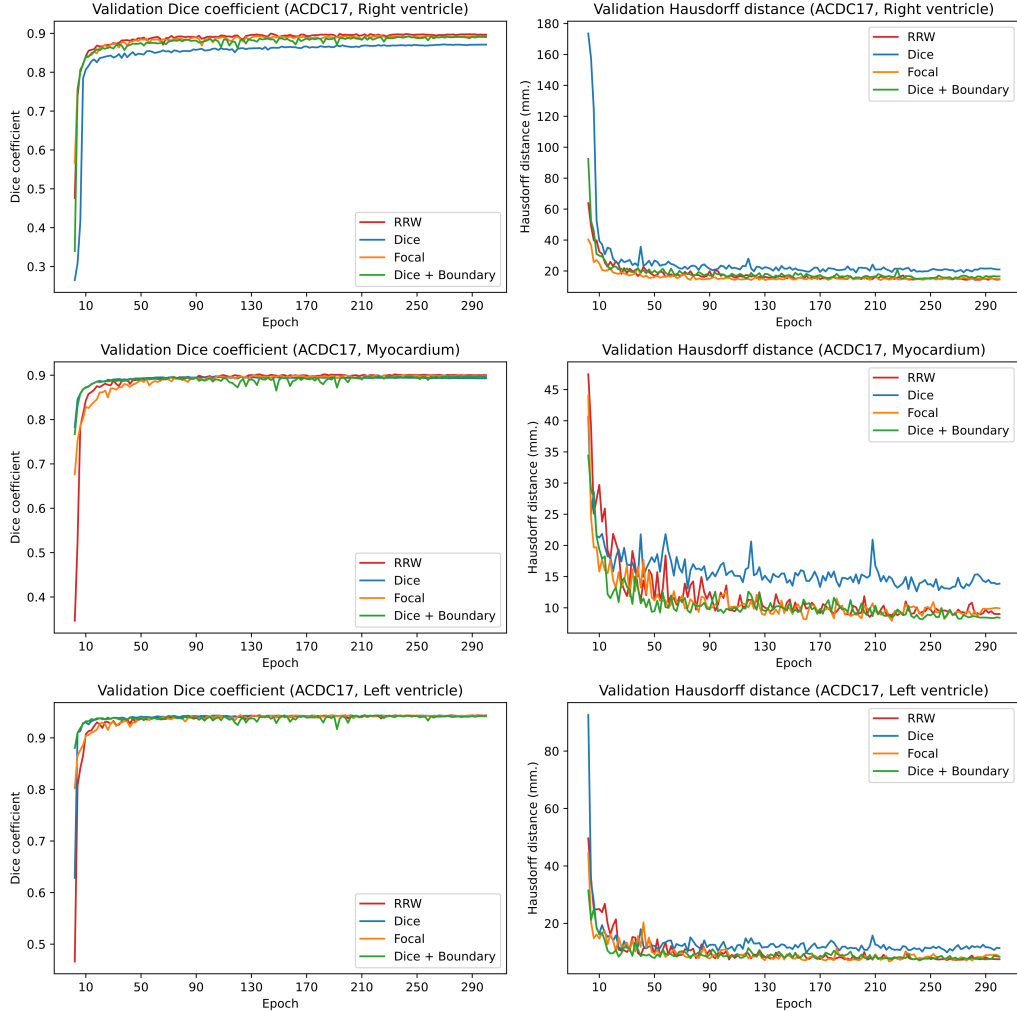


Figure 7: Validation Dice coefficient (left) and Hausdorff distance (right) for all non-background classes in ACDC17 dataset. Values are averages across 3 independent runs.

## B.2. BraTS18 Dataset

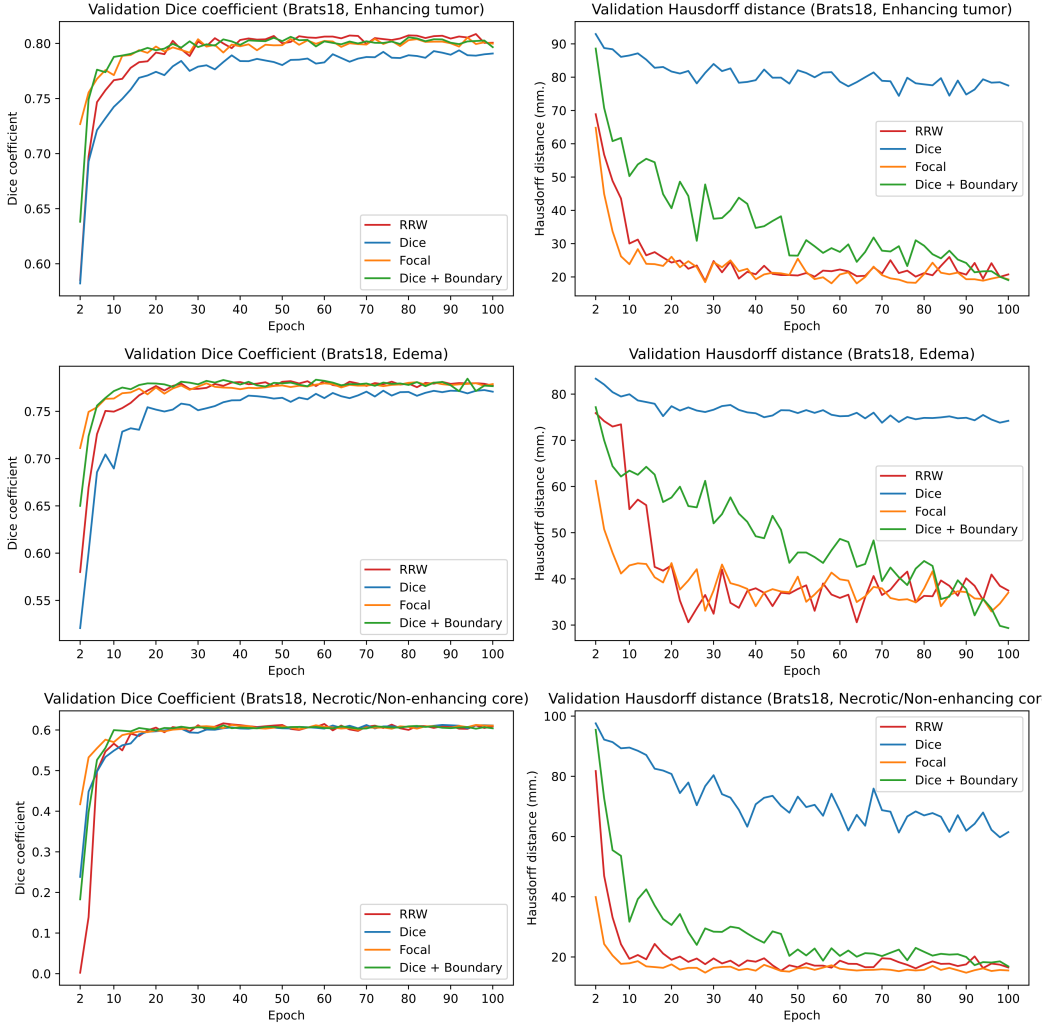


Figure 8: Validation Dice coefficient (left) and Hausdorff distance (right) for all non-background classes in BraTS18 dataset. Values are averages across 3 independent runs.

### B.3. KitTS19 Dataset

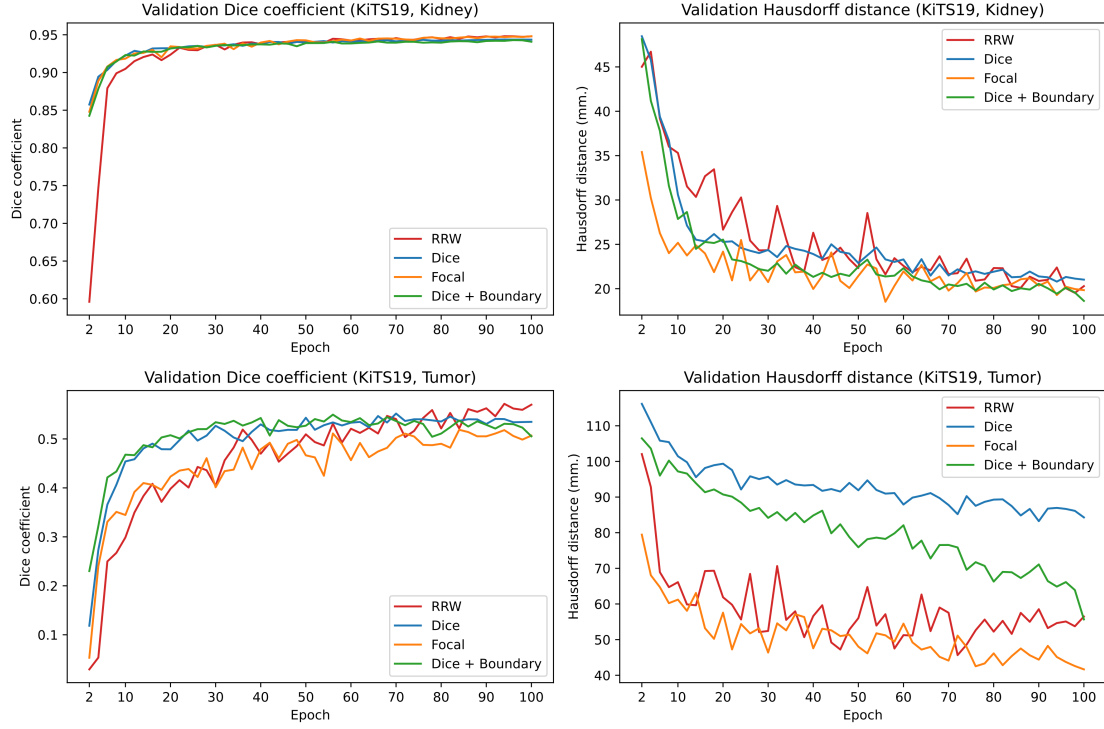


Figure 9: Validation Dice coefficient (left) and Hausdorff distance (right) for all non-background classes in KitTS19 dataset. Values are averages across 3 independent runs.